2752 Vol. 44, No. 11 / 1 June 2019 / Optics Letters Letter

Optics Letters

Dynamically tunable bowtie nanoantennas based on the phase transition of vanadium dioxide

FANG-ZHOU SHU,[1] LI-HENG ZHANG,[1] JIA-NAN WANG,[1] RU-WEN PENG,[1,2] REN-HAO FAN,[1] DONG-XIANG QI,[1] AND MU WANG[1,3]

[1]National Laboratory of Solid State Microstructures, School of Physics, and Collaborative Innovation Center of Advanced Microstructures, Nanjing University, Nanjing 210093, China
[2]e-mail: rwpeng@nju.edu.cn
[3]e-mail: muwang@nju.edu.cn

Received 15 February 2019; revised 13 April 2019; accepted 27 April 2019; posted 29 April 2019 (Doc. ID 360311); published 23 May 2019

The plasmonic nanoantenna has attracted intensive attention over the last decades owing to its unique optical response. Although various nanoantennas have been designed, so far very few efforts have been devoted to their dynamic tunability. Here we present a study on dynamically tunable bowtie nanoantennas integrated on a vanadium dioxide thin film with a thermal phase transition. The insulator–metal transition of vanadium dioxide changes its electric feature and permittivity; hence, the resonance of the bowtie nanoantennas is actively tuned by varying the temperature of the device. Further, by adjusting the gap of the bowtie and the edge size of the nanotriangle at a different temperature, the shift of the resonant wavelength of the nanoantenna has been found to increase for a larger triangle edge size, but less dependent on the gap width. The features suggest that VO_2-integrated nanoantennas may have applications in dynamically tunable high-harmonic generation, single-molecule fluorescence enhancement, and nanolasers.

https://doi.org/10.1364/OL.44.002752

The plasmonic nanoantenna has been extensively investigated in the past decades [1,2]. These artificial structures confine the electromagnetic field in subwavelength dimensions and are able to release radiation from localized sources to the far field [1,2]. So far for different purposes, various types of nanoantennas have been designed, including single nanospheres and nanorods [3,4], nanosphere and nanorod dimers [5,6], Yagi-Uda nanoantennas [7,8], and bowtie nanoantennas [9,10]. Among these structures, the bowtie nanoantenna has been extensively investigated owing to its superior localized field enhancement and spatial gap confinement. These properties arise from the combination of localized surface plasmon in the sharp-tipped geometries and the electrodynamic coupling between two arms of the antenna [11]. Therefore, they can be applied for high-harmonic generation [12], single-molecule fluorescence enhancements [13], enhanced Raman spectroscopy [14], and nanolasers [15].

Recently, active plasmonic nanoantennas have attracted much attention [16]. By combining plasmonic nanoantennas with tunable materials, such as graphene [17], liquid crystals [18], transparent conducting oxides [19], or phase-transition materials [20–23], the optical properties of plasmonic nanoantennas can be dynamically tuned by changing the voltage or temperature. However, despite the intensive studies on active plasmonic nanoantennas, very few efforts have been devoted to tunable bowtie nanoantennas [24,25], and the tunable range reported in previous works remains small. In this paper, we try to integrate bowtie nanoantennas with vanadium dioxide (VO_2) thin film to realize large tunable ranges. It has been known that VO_2 is a monoclinic insulator at room temperature and transforms to a rutile metal above 68°C [26]. The phase transition of VO_2 is first-order and reversible, during which its electrical and optical properties experience large changes. Consequently, it has been widely applied in field-effect transistors [27], tunable plasmonic colors and polarizers [28,29], active metamaterials [30–32], and waveguide switches [33]. Recently, active terahertz nanoantennas based on VO_2 phase transition have been achieved [34], and switchable nanoantennas utilizing VO_2 have been proposed based on simulations [35].

In this work, we demonstrated dynamically tunable bowtie nanoantennas integrated with a VO_2 thin film by changing the temperature. First, we investigated the optical properties of the VO_2 thin film at different temperatures. Then, we designed a composite nanostructure by integrating bowtie nanoantennas with the VO_2 thin film, and we investigated their optical properties at different temperatures with x- and y-polarized incidence. Next, we changed the gap width of the bowtie nanoantenna and examined the dependence of its optical properties with temperature. Finally, we varied the triangle size of the bowtie nanoantenna and investigated the associated optical response at different temperatures.

We first analyzed the optical properties of the VO_2 thin film. A 100-nm-thick VO_2 film has been fabricated on a glass substrate by electron-gun evaporation of vanadium followed by thermal annealing in the O_2 atmosphere [28,29]. Figure 1(a) shows the scanning electron microscopy (SEM) image of the VO_2 thin film, indicating that the film was featured with many nanoparticles on the top surface. We also measured the Raman spectra of VO_2 thin film at 20°C and 80°C, respectively, as presented in Fig. 1(b). Several characteristic peaks were identified in the 20°C spectrum as A_g modes at 195, 222, 392, and

0146-9592/19/112752-04 Journal

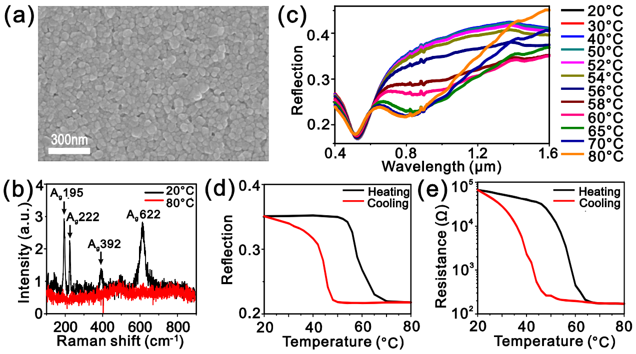

Fig. 1. (a) SEM image of 100-nm-thick VO_2 film on glass substrate. At different temperatures, the characterization of the 100-nm-thick VO_2 film is shown: (b) Raman spectra, (c) reflection spectra, (d) reflection intensities at the wavelength of 800 nm, and (e) electrical resistance during heating and cooling processes.

622 cm^{-1}, respectively, indicating the monoclinic structure of VO_2. These peaks, however, disappeared at 80°C, signifying the insulator–metal transition of VO_2 [36]. Figure 1(c) shows the reflection spectra of the VO_2 thin film at different temperatures, which were measured by a temperature-controlled stage with a UV-visible near-infrared (NIR) microspectrophotometer with normal and unpolarized incidence. One may find that the reflection of VO_2 thin film changed continuously when temperature increased due to the phase transition of VO_2 [26]. The reflection changed much more significantly in the NIR spectrum. We also measured the reflection spectra of the VO_2 thin film in heating and cooling processes at the wavelength of 800 nm, respectively, as presented in Fig. 1(d). Figure 1(e) shows the electrical resistance of the 100-nm-thick VO_2 film at different temperatures. The variations in both the reflection and the electrical resistance with temperature formed the hysteresis due to different nucleation processes occurring in the phase transition between the heating and cooling processes. The phase-transition temperature of the VO_2 thin film we detected was approximately 58°C. This was lower than its typical critical temperature, which might be influenced by both oxygen vacancies [26] in the sample and lattice mismatch between the VO_2 film and glass substrate.

Since the optical properties of the VO_2 thin film varied dramatically in the NIR spectrum across the phase-transition point, a combination of a bowtie nanoantenna and VO_2 thin film can thus realize a tunable nanoantenna system. We introduced here integrated bowtie nanoantennas with VO_2 thin film, as illustrated in Fig. 2(a). The upper layer is a two-dimensional periodic array of gold bowtie nanoantennas, which are made of two equilateral triangles separated by a gap. Due to the nonzero imaginary part of the refractive index of VO_2 in both insulating and metallic phases at the NIR frequencies, a 30-nm-thick silicon dioxide (SiO_2) layer was used to separate the VO_2 thin film from the bowtie nanoantenna array in order to reduce electromagnetic loss [37]. Glass was used as the substrate. In the experiments, the samples were fabricated as follows: a 30-nm-thick SiO_2 film was deposited onto the 100-nm-thick VO_2 film by electron-gun evaporation. Then, periodic bowtie nanoantenna arrays were defined using standard electron beam lithography followed by a gold lift-off procedure. Figure 2(b) is the SEM micrograph of a sample with a triangle length of 280 nm, gap width of 20 nm,

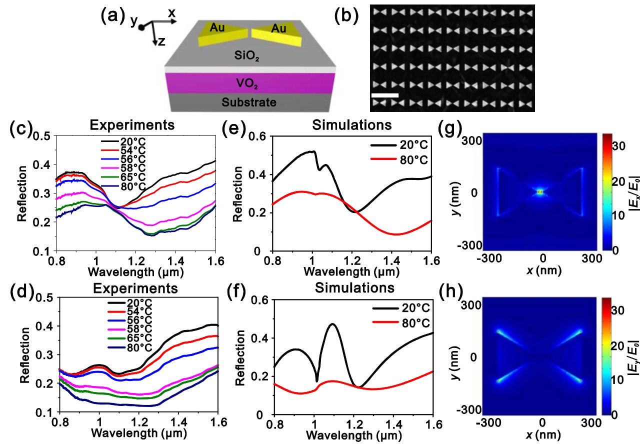

Fig. 2. (a) Model of the composite structure. (b) SEM image of a sample with a triangle length of 280 nm and gap width of 20 nm; the scale bar represents 1 μm. Measured reflection spectra of the sample at different temperatures under (c) *x*- and (d) *y*-polarized incidence. Simulated reflection spectra of the sample at different temperatures under (e) *x*- and (f) *y*-polarized incidence. In-plane electric field distribution with VO_2 in the insulating phase for (g) *x*-polarized incidence and (h) *y*-polarized incidence.

thickness of 50 nm, and spatial periodicity of 700 nm. We measured the reflection spectra of the fabricated sample on a temperature-controlled stage with a UV-visible-NIR microspectrophotometer with *x*- and *y*-polarized incidence. Figure 2(c) shows the reflection spectra of the sample at different temperatures with *x*-polarized incidence. A dip can be identified at 1110 nm in the 20°C spectrum, which redshifted as the temperature increased. When the sample was heated to 80°C, the dip shifted to 1280 nm. Figure 2(d) presents the reflection spectra of the sample at different temperatures with *y*-polarized incidence. A similar dip was identified at 1100 nm at 20°C, which also redshifted as the temperature increased. When the sample was heated to 80°C, the dip shifted to 1250 nm. Because the phase transition of VO_2 is reversible, when the sample was cooled to room temperature, the reflection spectra returned to their original states for both *x*- and *y*-polarized incidence.

To confirm these experimental observations, we simulated the reflection spectra of the sample using the finite-difference time-domain software (FDTD Solutions) from Lumerical Inc. The complex refractive index data of VO_2 in the metallic and dielectric phases were taken from the Ref. [37], and the complex refractive index for Au was interpolated from Ref. [38]. Figure 2(e) shows the calculated reflection spectra of the sample at 20°C and 80°C with *x*-polarized incidence. A dip appeared at 1220 nm at 20°C, which shifted to 1430 nm at 80°C. Figure 2(f) shows the calculated reflection spectra of the sample with *y*-polarized incidence at 20°C and 80°C, respectively. Similarly, one may find a dip at 1230 nm at 20°C, which shifted to 1300 nm at 80°C. The calculated results reasonably agree with the experimental data.

To better understand the features of the reflection spectra, we analyzed the electric field distributions at the observed dips. Figure 2(g) illustrates the FDTD-simulated electric field distribution at 1220 nm with VO_2 in the insulating phase for *x*-polarized incidence. In this structure, the gap of the bowtie nanoantennas is about 20 nm, and the coupling of two triangle tips is not strong enough; therefore, two separated hot spots appear within the gap [12,24]. By further shrinking this gap, these two hot spots will be merged. The refractive index of VO_2 changed with varying temperature. When the temperature increased, the wavelength of the localized surface plasmon became larger, leading to the redshift in the dip. Figure 2(h) illustrates the FDTD-simulated electric field distribution at 1230 nm with VO_2 in the insulating phase for *y*-polarized incidence. One may find that the electric field mainly concentrated at the edge of two equilateral triangles, which was due to the excitation of localized surface plasmon on each equilateral triangle. The dip also shifted with increasing temperature due to the variation in the refractive index of VO_2. However, the wavelength shift of the dip was larger in the scenario of *x*-polarized incidence than that of the *y*-polarized incidence. The effect was due to the higher electric field enhancement for *x*-polarized incidence than that for *y*-polarized incidence.

It has been well known that the optical properties of bowtie nanoantennas can be tuned by adjusting the geometric parameters [39,40]. Therefore, it is possible to vary the gap and triangle size to tune the optical properties at different temperatures across the phase transition of VO_2 in our VO_2-integrated bowtie nanoantennas. First, we examined the effect of gap width on the optical properties at different temperatures. We fabricated six samples with different gap widths ranging from 10 nm to 60 nm, keeping the other parameters identical to the sample in Fig. 2(b). Figures 3(a) and 3(b) show the measured reflection spectra of these samples with different gap widths by *x*-polarized incidence at 20°C and 80°C, respectively. The dip in the reflection spectra blueshifted as the gap width increased, due to the decrease in coupling between the two equilateral triangles [40]. Figure 3(c) illustrates the variation in the dip position as a function of gap width at 20°C and 80°C, respectively. The dip blueshifted slowly as the gap width increased. By changing temperature, this process does not change very much, characterized by almost invariant separation between the red and dark lines in Fig. 3(c). To confirm these experimental results, we calculated the reflection spectra of the samples with different gap widths and temperature under *x*-polarized incidence via FDTD simulation, and the results are shown for 20°C and 80°C in Figs. 3(d) and 3(e), respectively. Similar to the above experimental results, the dip in the reflection spectra blueshifted with increasing the gap width.

Figure 3(f) illustrates the variation in dip wavelength with gap width at 20°C and 80°C. Similar to the experimental observation, the dip blueshifted as the gap width increased, whereas the wavelength shift remained constant across nearly all gap widths for different temperatures.

We also investigated the effect of the triangle size of the bowtie nanoantenna on the optical properties. We fabricated six samples with different triangle sizes ranging from 200 to 300 nm, while keeping the other parameters the same as the sample in Fig. 2(b). Figures 4(a) and 4(b) show the measured reflection spectra of the samples with different triangle sizes with *x*-polarized incidence at 20°C and 80°C, respectively. We observed a redshift of the dip in the reflection spectra as increasing the triangle edge size. This was due to the increased retardation effects of the exciting electromagnetic field and the depolarization field inside the bowtie nanoantennas [40]. Figure 4(c) illustrates the variation in dip wavelength with the triangle size at 20°C and 80°C, respectively. The dip redshifted with increasing the size, whereas the shift of the resonant wavelength with temperature has been increased for the larger triangle size. To confirm these experimental observations, we calculated the reflection spectra of the samples with different triangle sizes at different temperatures with *x*-polarized incidence by FDTD simulation, and Figs. 4(d) and 4(e) show the results at 20°C and 80°C, respectively. Similar to the experimental results, a redshift occurred for the dip in the reflection spectra when the triangle size was increased. Figure 4(f) illustrates the variation of the dip position as a function of triangle size at 20°C and 80°C, respectively. Similar to the experimental results, the dip redshifted by increasing the triangle size, whereas the wavelength shift with temperature was larger at a larger triangle size. The calculated results were in agreement with the experimental observations except for some minor differences. It should be mentioned that there exist some discrepancies between the calculated and experimental results (to see Figs. 2–4). Those discrepancies mainly come from the following facts: (i) the fabricated VO_2 and SiO_2 films are inhomogeneous, where some grains and defects occur; and (ii) the nanobowties are a little irregular in experiments instead of perfect triangles supposed in the simulations.

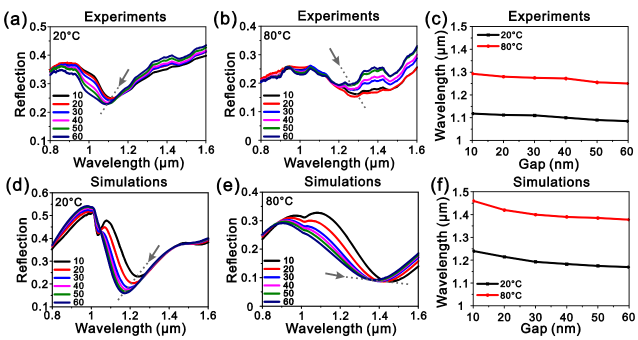

Fig. 3. Measured reflection spectra of samples with different gap widths under *x*-polarized incidence at (a) 20°C and (b) 80°C. (c) Variation in the marked-dip wavelength in (a) and (b) with a gap width at 20°C and 80°C. Simulated reflection spectra of samples with different gap widths under *x*-polarized incidence at (d) 20°C and (e) 80°C. (f) Variation in the marked-dip wavelength in (d) and (e) with a gap width at 20°C and 80°C.

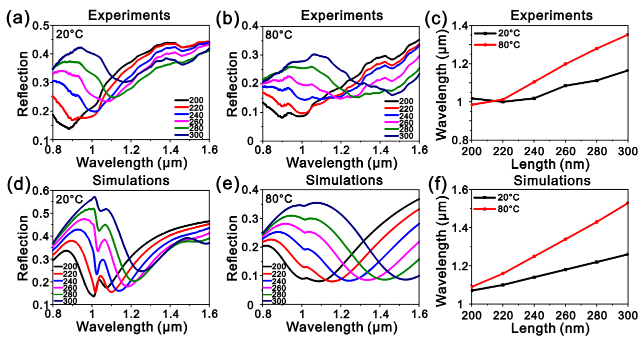

Fig. 4. Measured reflection spectra of samples with different triangle lengths under *x*-polarized incidence at (a) 20°C and (b) 80°C. (c) Variation in dip wavelength in (a) and (b) with a triangle length at 20°C and 80°C. Simulated reflection spectra of samples with different triangle lengths under *x*-polarized incidence at (d) 20°C and (e) 80°C. (f) Variation in dip wavelength in (d) and (e) with a triangle length at 20°C and 80°C.

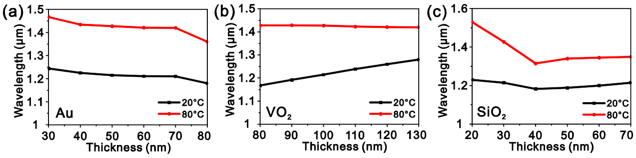

Fig. 5. Wavelength variation of the reflection dip in simulated reflection spectra at 20°C and 80°C with increasing the thickness of (a) Au triangles, (b) VO_2 layer, and (c) SiO_2 layer, respectively.

Besides, with increasing the thickness of the Au triangles, the VO_2 layer, and the SiO_2 layer, respectively, in the device, the resonant wavelength of the nanoantenna also changes at different temperatures 20°C and 80°C (as shown in Fig. 5). Particularly for a thicker SiO_2 layer (below 40 nm), the dip blueshifts a little bit at 20°C, whereas it blue shifts dramatically at 80°C.

In conclusion, we have demonstrated dynamically tunable bowtie nanoantennas integrated with VO_2 thin film. The resonant wavelength of the bowtie nanoantennas can be effectively tuned by changing the device temperature. It is the variation of the refractive index of VO_2 caused by the insulator–metal transition that plays a crucial role in controlling the response of the system. The shift of the resonant wavelength with temperature has been increased for a larger triangle size, whereas this shift is nearly independent of the gap width of the bowtie nanoantenna. The approach to use VO_2 to achieve an active nanoantenna system can be universal. We anticipate that VO_2-integrated nanoantennas will be enlightening for many applications, such as tunable high-harmonic generation, single-molecule fluorescence enhancements, and nanolasers.

Funding. National Key R&D Program of China (2017YFA0303702); National Natural Science Foundation of China (NSFC) (11634005, 11674155, 11604143, 11621091); "333 Project" from Jiangsu province (BRA2016350).

REFERENCES

1. L. Novotny and N. van Hulst, Nat. Photonics **5**, 83 (2011).
2. P. Biagioni, J.-S. Huang, and B. Hecht, Rep. Prog. Phys. **75**, 024402 (2012).
3. P. Anger, P. Bharadwaj, and L. Novotny, Phys. Rev. Lett. **96**, 113002 (2006).
4. A. Mohammadi, V. Sandoghdar, and M. Agio, New J. Phys. **10**, 105015 (2008).
5. P. Mühlschlegel, H.-J. Eisler, O. J. F. Martin, B. Hecht, and D. W. Pohl, Science **308**, 1607 (2005).
6. P. Ghenuche, S. Cherukulappurath, T. H. Taminiau, N. F. van Hulst, and R. Quidant, Phys. Rev. Lett. **101**, 116805 (2008).
7. A. G. Curto, G. Volpe, T. H. Taminiau, M. P. Kreuzer, R. Quidant, and N. F. van Hulst, Science **329**, 930 (2010).
8. T. Kosako, Y. Kadoya, and H. F. Hofmann, Nat. Photonics **4**, 312 (2010).
9. D. P. Fromm, A. Sundaramurthy, P. J. Schuck, G. Kino, and W. E. Moerner, Nano Lett. **4**, 957 (2004).
10. J. N. Farahani, D. W. Pohl, H.-J. Eisler, and B. Hecht, Phys. Rev. Lett. **95**, 017402 (2005).
11. K. D. Ko, A. Kumar, K. H. Fung, R. Ambekar, G. L. Liu, N. X. Fang, and K. C. Toussaint, Nano Lett. **11**, 61 (2011).
12. S. Kim, J. Jin, Y.-J. Kim, I.-Y. Park, Y. Kim, and S.-W. Kim, Nature **453**, 757 (2008).
13. A. Kinkhabwala, Z. Yu, S. Fan, Y. Avlasevich, K. Müllen, and W. E. Moerner, Nat. Photonics **3**, 654 (2009).
14. N. A. Hatab, C.-H. Hsueh, A. L. Gaddis, S. T. Retterer, J.-H. Li, G. Eres, Z. Zhang, and B. Gu, Nano Lett. **10**, 4952 (2010).
15. J. Y. Suh, C. H. Kim, W. Zhou, M. D. Huntington, D. T. Co, M. R. Wasielewski, and T. W. Odom, Nano Lett. **12**, 5769 (2012).
16. N. Jiang, X. Zhuo, and J. Wang, Chem. Rev. **118**, 3054 (2018).
17. Y. Yao, M. A. Kats, P. Genevet, N. Yu, Y. Song, J. Kong, and F. Capasso, Nano Lett. **13**, 1257 (2013).
18. A. Abass, S. R.-K. Rodriguez, T. Ako, T. Aubert, M. Verschuuren, D. V. Thourhout, J. Beeckman, Z. Hens, J. G. Rivas, and B. Maes, Nano Lett. **14**, 5555 (2014).
19. M. Z. Alam, S. A. Schulz, J. Upham, I. D. Leon, and R. W. Boyd, Nat. Photonics **12**, 79 (2018).
20. A.-K. U. Michel, D. N. Chigrin, T. W. W. Maß, K. Schönauer, M. Salinga, M. Wuttig, and T. Taubner, Nano Lett. **13**, 3470 (2013).
21. M. A. Kats, R. Blanchard, P. Genevet, Z. Yang, M. M. Qazilbash, D. N. Basov, S. Ramanathan, and F. Capasso, Opt. Lett. **38**, 368 (2013).
22. S. K. Earl, T. D. James, T. J. Davis, J. C. McCallum, R. E. Marvel, R. F. Haglund, and A. Roberts, Opt. Express **21**, 27503 (2013).
23. J. Tian, H. Luo, Y. Yang, F. Ding, Y. Qu, D. Zhao, M. Qiu, and S. I. Bozhevolnyi, Nat. Commun. **10**, 396 (2019).
24. Q. Wang, L. Liu, Y. Wang, P. Liu, H. Jiang, Z. Xu, Z. Ma, S. Oren, E. K. C. Chow, M. Lu, and L. Dong, Sci. Rep. **5**, 18567 (2015).
25. F. Laible, D. A. Gollmer, S. Dickreuter, D. P. Kern, and M. Fleischer, Nanoscale **10**, 14915 (2018).
26. K. Liu, S. Lee, S. Yang, O. Delaire, and J. Wu, Mater. Today **21**(8), 875 (2018).
27. M. Nakano, K. Shibuya, D. Okuyama, T. Hatano, S. Ono, M. Kawasaki, Y. Iwasa, and Y. Tokura, Nature **487**, 459 (2012).
28. F.-Z. Shu, F.-F. Yu, R.-W. Peng, Y.-Y. Zhu, B. Xiong, R.-H. Fan, Z.-H. Wang, Y. Liu, and M. Wang, Adv. Opt. Mater. **6**, 1700939 (2018).
29. Z.-Y. Jia, F.-Z. Shu, Y.-J. Gao, F. Cheng, R.-W. Peng, R.-H. Fan, Y. Liu, and M. Wang, Phys. Rev. Appl. **9**, 034009 (2018).
30. T. Driscoll, H.-T. Kim, B.-G. Chae, B.-J. Kim, Y.-W. Lee, N. M. Jokerst, S. Palit, D. R. Smith, M. D. Ventra, and D. N. Basov, Science **325**, 1518 (2009).
31. M. Liu, H. Y. Hwang, H. Tao, A. C. Strikwerda, K. Fan, G. R. Keiser, A. J. Sternbach, K. G. West, S. Kittiwatanakul, J. Lu, S. A. Wolf, F. G. Omenetto, X. Zhang, K. A. Nelson, and R. D. Averitt, Nature **487**, 345 (2012).
32. K. Dong, S. Hong, Y. Deng, H. Ma, J. Li, X. Wang, J. Yeo, L. Wang, S. Lou, K. B. Tom, K. Liu, Z. You, Y. Wei, C. P. Grigoropoulos, J. Yao, and J. Wu, Adv. Mater. **30**, 1703878 (2018).
33. P. Markov, R. E. Marvel, H. J. Conley, K. J. Miller, R. F. Haglund, and S. M. Weiss, ACS Photon. **2**, 1175 (2015).
34. M. Seo, J. Kyoung, H. Park, S. Koo, H.-S. Kim, H. Bernien, B. J. Kim, J. H. Choe, Y. H. Ahn, H.-T. Kim, N. Park, Q.-H. Park, K. Ahn, and D.-S. Kim, Nano Lett. **10**, 2064 (2010).
35. P. B. Savaliya, A. Thomas, R. Dua, and A. Dhawan, Opt. Express **25**, 23755 (2017).
36. H.-T. Kim, B.-G. Chae, D.-H. Youn, G. Kim, K.-Y. Kang, S.-J. Lee, K. Kim, and Y.-S. Lim, Appl. Phys. Lett. **86**, 242101 (2005).
37. H. W. Verleur, A. S. Barker, and C. N. Berglund, Phys. Rev. **172**, 788 (1968).
38. P. B. Johnson and R. W. Christy, Phys. Rev. B **6**, 4370 (1972).
39. H. Fischer and O. J. F. Martin, Opt. Express **16**, 9144 (2008).
40. M. Kaniber, K. Schraml, A. Regler, J. Bartl, G. Glashagen, F. Flassig, J. Wierzbowski, and J. J. Finley, Sci. Rep. **6**, 23203 (2016).